Controllable Heterogeneous Seeding Induced Crystallization for High-Efficiency FAPbI$_3$-based perovskite solar cells over 24%

Hengkai Zhang[1,2,3], Zhiwei Ren[1,2], Kuan Liu[1,2], Minchao Qin[4], Zehan Wu[5], Dong Shen[6], Yaokang Zhang[7], Hrisheekesh Thachoth Chandran[1,2], Jianhua Hao[5], Chun-sing Lee[6], Xinhui Lu[4], Zijian Zheng[7], Jinsong Huang[3], Gang Li[1,2]*

Affiliations:

[1]Department of Electronic and Information Engineering, Research Institute for Smart Energy (RISE), The Hong Kong Polytechnic University, Hung Hom, Kowloon, Hong Kong, China

[2]The Hong Kong Polytechnic University Shenzhen Research Institute, Shenzhen 518057, China

[3]Department of Applied Physical Sciences, University of North Carolina at Chapel Hill, Chapel Hill, NC, USA

[4]Department of Physics, The Chinese University of Hong Kong, New Territories, Hong Kong, China

[5]Department of Applied Physics, The Hong Kong Polytechnic University, Hung Hom, Kowloon, Hong Kong, China

[6]Center of Super-Diamond and Advanced Films (COSDAF) and Department of Chemistry, City University of Hong Kong, Kowloon, Hong Kong, China

[7]Laboratory for Advanced Interfacial Materials and Devices, Research Centre for Smart Wearable Technology, Institute of Textiles and Clothing, The Hong Kong Polytechnic University, Hung Hom, Kowloon, Hong Kong, China

* Correspondence author. Email: gang.w.li@polyu.edu.hk (G.L.)

Keywords: perovskite solar cell, α-FAPbI$_3$, heterogeneous seeding induced crystallization

Abstract

The addition of small seeding particles into a supersaturated solution is one effective approach to increase the crystallization rates to obtain high-quality semiconductor material. However, limited study was conducted on this approach for the fabrication of perovskite solar cells, a. Here, we propose a new strategy - heterogeneous seeding-induced crystallization (hetero-SiC) to assist the growth of FAPbI$_3$-based perovskite. In this work, the (t-Bu)$_2$PMeHBF$_4$ is directly introduced into the precursor which forms a low solubility complex with PbI$_2$. The low solubility complex can serve as the seed to induce crystallization of perovskite during the solvent evaporation process. The hetero-SiC process is proven to be one effective way to manipulate the nucleation process and crystal growth of perovskite which is visualized by several in situ measurement tools. The hetero-SiC greatly improves the film quality, reduces the film defects, and suppression the

non-radiative recombination. The hetero-SIC device exhibits outstanding performance with 24.0% PCE, well over the control device of 22.2% PCE. The stability of hetero-SiC PSCs under light illumination is also improved which maintains 84% of initial performance after 1400h light illumination.

Introduction

Organic-inorganic metal halide perovskite solar cells (PSCs) have attracted great interest over the last decades and obtained a power conversion efficiency of ~~over~~ certified 25.7%.[1] The solution-processed fabrication of PSCs provides a huge advantage over other techniques to obtain cost-effective solar cells with a facile manufacturing process.[2] As a solution process technique, the slow crystallization process of perovskite will lead to a non-uniform and non-fully covered film with large crystals.[2-4] Several strategies were introduced to manipulate the perovskite crystallization, including anti-solvent qunching[3, 5], gas quenching[6], vacuum quenching[7], elevated temperature coating, and so on. The above-mentioned approaches are majority focused on facilitating the evaporation of solvent to promote a rapid saturation and lead to faster crystallization.

A~~Besides, a~~dding small crystal seeding is a classical approach in the semiconductor area to obtain ~~good~~ high quality semiconductor material (Si and GaAs) with reduced defect density under a high growth speed.[8] Inspired by this, the seed-~~assisted growth~~induced crystallization is ~~widely used~~also adopted in PSCs fabrication[9-17]. The seed-induced crystallization is believed to be one effective approach to modulating the film formation process by reducing the critical Gibbs free energy of nucleation.[8] Based on the variety of seed material and target material, the ~~seeding~~ seeding-induced crystallization (SiC) can be divided into heterogeneous and homogeneous (hetero-SiC and homo-SiC). The homogeneous-seeding induced crystallization (homo-SiC) of perovskite is one important approach to enhancing the film quality and reducing defect density.[9-15] Typically, the seeds applied in homo-SIC exhibit a lattice-matching with target perovskite to a certain extend. The homo-S~~I~~iC exhibits unique glamor in the area of PSCs, especially for the two-step fabrication of perovskite. Sargent's group reported embedding perovskite seed crystal (CsPbI$_3$) in PbI$_2$ film which acts as nuclei to facilitate crystallization during the two-step fabrication of perovskite.[10] With the perovskite seed crystal, the PSCs show a striking improvement in both stability and performance. On the basis of this method, Zhao's group achieves better device performance by replacing CsI with CsCl to serve as the seed in the PbI$_2$ precursor ink.[12] They found the Cl$^-$ could retard the crystallization process and reduce the nucleation center which lead to an enlarge grain size and reduced defects. Besides these works, multiple seed materials were developed and added in the PbI$_2$ precursor ink to serve as the seed in the two-step deposition method and achieve great performance enhancement, including mixed perovskite seed of Cs and Rb cations[13, 14], Br-rich perovskite seed[15], and tert-butylpyridine (TBP)[16]. Apart from introducing seed in PbI$_2$ ink of the two-step method, the seed assistant growth approach was also applied in one step deposition method. Chen's group developed one intermixing-seeded growth approach with the addition of MAI-capped PbS nanoparticles in the perovskite precursor solution.[17] The MAI-capped PbS can be functioned as effective heterogeneous nucleation sites to promote the formation of the inorganic framework of perovskite lattice structures, leading to enhanced film coverage and improved performance. On the basis of

this work, Chen's group further revealed the "catalytic" role of PbS seed nanoparticle that the PbS NCs can catalyze the conversion of the intermediate phase into perovskite crystals by reducing activation energy.[18] Meanwhile, alkali additives (KPb_2Br_5) was added in the precursor ink as crystallization seed to enable highly crystalline large-area perovskite film via slot-die coating.[19] CdSe colloidal quantum dots was also reported to serve as crystallization seeds to modulate the nucleation and crystal growth processes.[20]

Rather than direct adding seed to the precursor, the formation seed template at the bottom interface was also reported as an effective approach for the crystallization modulation. Gratzel's group reported a simple approach by- using a pre-deposited PMMA template as the seeds to induce the growth of high-quality perovskite film.[21] The PMMA template was found to enable heterogeneous nucleation (hetero-SiC) of perovskite film with few defects and larger oriented grains. Han' group reported a perovskite crystal array (PCA) method to assist the growth of the perovskite absorption layer.[22] The patterned perovskite crystal array is regularly distributed on the substrate and served as templated crystal, which induced a well-organized upward crystallization process.

The study on the seed assistant perovskite growth indeed acquires good progress. However, the majority of works were focused on the two-step deposition method and the study of the one-step deposition method is limited. Therefore, However, we start to find a facile strategy to manipulate the crystallization process by directly introducing the seed material (non-perovskite material) into the precursor solution was rarely reported in one step solution-processed method of perovskite fabrication. [19,20] Its difficulties The key challenge of it lies in the selection of seeding material, where an optimized material solubility should be selected. If the seed material solubility is too low, the seeds are precipitated in the precursor and will greatly detriment film quality which makes it difficult to obtain a smooth and uniform film. While for a high solubility material, it cannot serve as the seeds for perovskite crystallization.

The organic ionic compounds with chemical stable organic cation were widely used as an additive for the perovskite. Several groups have revealed the ionic liquid/salts ([BMIM]BF_4, [BMP]BF_4, et al) could passivate the defects and work as stabilizers for PSCs.[23-25] The incorporation of the ionic compound in the perovskite absorber could suppress deep trap states, boost PSCs' performance and operation stability.[23, 24, 26, 27] The organic ionic compounds are also used as interface modifiers for PSCs, such as hole or electron-transporting layer/perovskite absorber interface.[24, 25, 28-31] Due to these advantages, we start to select from the group of organic ionic compounds and find di-tert-butyl(methyl)phosphonium tetrafluoroborate ((t-Bu)$_2$PMeHBF_4) can form low solubility complex with PbI_2 in majority popular solvent for perovskite precursor, including DMF, DMSO, and 2-Methoxyethanol. Furthermore, we systematically analyze the whole nucleation and growth process of perovskite with (t-Bu)$_2$PMeHBF_4 by in situ characterization techniques (in situ absorption, XRD and et. al), providing a new understanding of the seeded perovskite growth. At last, the hetero-SiC strategy formed perovskite films exhibit high-quality, low trap density, and enlarged grain size. The hetero-SiC PSCs demonstrate outstanding performance with a PCE of 24.0% (over the control device with 22.2%). The hetero-SiC PSCs also exhibit a greatly enhanced operation stability which maintains 84% of initial performance after 1400h light illumination.

Results and discussion

The (t-Bu)$_2$PMeHBF$_4$ is one low-cost widely used electron-rich ligand (ionic salts) for palladium-catalyzed cross-coupling reactions. The chemical structure of (t-Bu)$_2$PMeHBF$_4$ is shown in **Fig. 1B** inset. In this work, we demonstrate a heterogeneous-seeding induced crystallization (**hetero-SiC**) approach to manipulate the crystallization process of perovskite via this low-cost ionic salts (t-Bu)$_2$PMeHBF$_4$. In this approach, a small amount of (t-Bu)$_2$PMeHBF$_4$ is added into the precursor of (FAPbI$_3$)$_{0.93}$(MAPbBr$_3$)$_{0.04}$(CsPbI$_3$)$_{0.03}$ perovskite - FAMACs perovskite. The additive (t-Bu)$_2$PMeHBF$_4$ can react with PbI$_2$ to form a low solubility complex. The low solubility complex will precipitate as nuclei seeds which facilitate the growth of perovskite crystals. The crystallization process of perovskite via hetero-SiC can be explained by the classical model of Gibbs free energy.

In classical theory, the crystallization of perovskite involved two important processes: nucleation and growth.[2] The film quality is highly related to the rates of these two processes. At first, the nucleation of fine particles is initiated from the supersaturated state.[2] For conventional homogeneous nucleation, the nuclei formation can be considered as a thermodynamical equilibrium where the total free energy (ΔG) of a spherical particle is equal to the sum of the surface free energy (ΔG$_s$) and the bulk free energy (ΔG$_v$). In a supersaturated solution, the ΔG$_s$ is positive quantity proportional to r^2 and ΔG$_v$ is negative quantity proportional to r^3. The total free energy is defined as $\Delta G = \Delta G_S + \Delta G_V = 4\pi r^2 \gamma + \frac{4}{3}\pi r^3 \Delta G_v$, where γ is the surface energy between the supersaturated solution and crystalline surface and ΔG_v is the bulk free energy per unit volume. The formation of nuclei is strongly dependent on the critical radius (r*): if the nuclei radii are smaller than r*, the nuclei are dissolved back into the solution; if the nuclei radii are greater than r*, the nuclei are thermodynamically stable and will grow further (**Fig. 1C**). With the hetero-SiC, the complex of PbI$_2$-(t-Bu)$_2$PMeBF$_4$ is pre-nucleated as the seeds (nucleation centers) of the following perovskite nucleation (**Fig. 1D**). The seeds could greatly reduce the interface energy and then the nucleation barrier of perovskite which allows the nucleation of perovskite nuclei occurs at a lower saturation.[2] While for the homogeneous nucleation, small and dense nuclei are gradually generated slowly during the solvent evaporation.[32-34]

The seeding in the precursor is characterized by the dynamic light scattering measurement. From the scattering spectral, we find the colloids exhibit two dominant distributions (**Fig. 1A**). With the addition of (t-Bu)$_2$PMeHBF$_4$, the colloids with the size between 100-300 nm (control precursor) are gradually grown to 400-2500 nm (precursor with 1 mol% additive) which indicates the growth of particle under different concentration of additive (peaks position shown in **Fig. 1A**). These large colloids from the control precursor are mainly coming from perovskite natural clustering. With (t-Bu)$_2$PMeHBF$_4$, the size of colloids gradually increases which is due to the generation of a low solubility complex. In comparison with control one, the precursor with 0.3 and 0.5 mol% (t-Bu)$_2$PMeHBF$_4$ also exhibit a lower intensity of spectral (particles size over 100nm) indicating a reduced nucleation center. This could be due to the small perovskite clusters being aggregated into large size nucleation centers with the assistance of the low solubility complex. From the optical image, we could also find amounts of low solubility white needle shape

precipitated in the precursor with 1 mol% (t-Bu)$_2$PMeHBF$_4$ (**Fig. 1B** inset photo). The XRD measurement was conducted onto the film with and without (t-Bu)$_2$PMeHBF$_4$. Compared with the control film, a new peak around 8.8^o is found on the XRD pattern of the film with (t-Bu)$_2$PMeHBF$_4$ (**Fig. 1B**) which is attributed to the newly formed white crystal. To reveal the origin of the new generated phase, the (t-Bu)$_2$PMeHBF$_4$ are added into the precursor solutions of PbI$_2$ and FAI (fig. S1). The white needle shape crystals only precipitate from the PbI$_2$ precursor solution with (t-Bu)$_2$PMeHBF$_4$. The XRD analysis also represents the same diffraction peak at 8.8^o from the (t-Bu)$_2$PMeHBF$_4$ -PbI$_2$ film (fig. S2). This indicates the newly generated phase is one complex of (t-Bu)$_2$PMeHBF$_4$-PbI$_2$. Furthermore, solutions with different ratios of (t-Bu)$_2$PMeHBF$_4$ and PbI$_2$ are also prepared. From the XRD pattern, we find a relatively pure phase with a negligible amount of residual PbI$_2$ with the ratio of 1:2 (PbI$_2$: (t-Bu)$_2$PMeHBF$_4$) (fig. S2). To obtain a smooth and uniform film, it is desirable to avoid the precipitation of complex in perovskite precursors. Therefore, we first surveyed and determined 0.3 mol% gave the best film quality and device performance, and thus we use it as the standard concentration in demonstrating the following nucleation process.

5
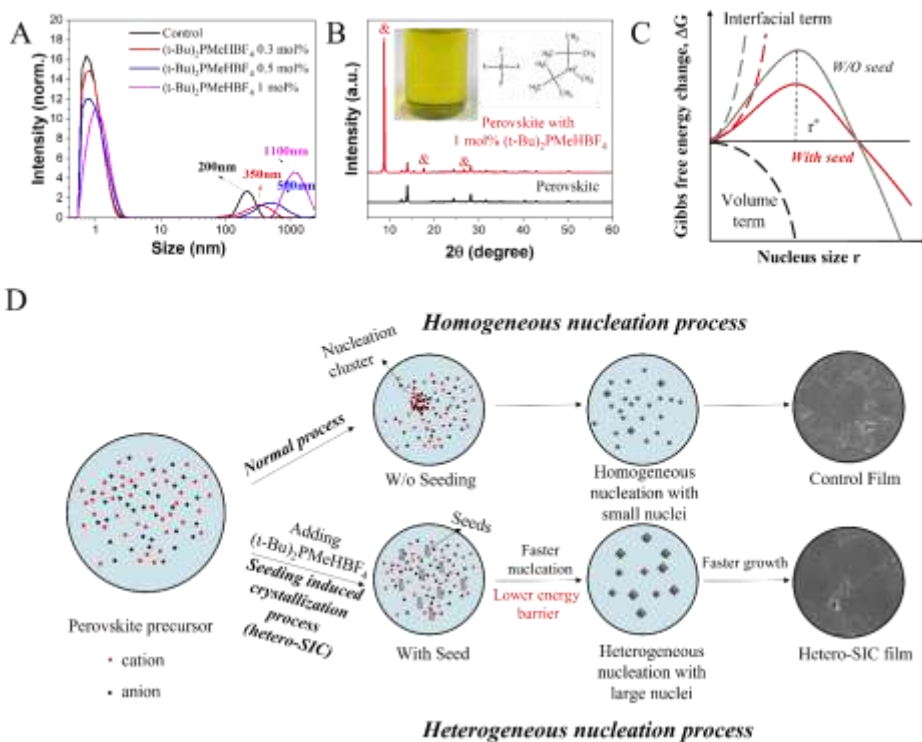
Fig. 1. Mechanism of hetero-seeding induced crystallization (hetero-SiC) by (t-Bu)$_2$PMeHBF$_4$. (A) Dynamic light scattering spectra of perovskite precursor with different concentration of di-tert-butyl(methyl)phosphonium tetrafluoroborate ((t-Bu)$_2$PMeHBF$_4$). The size indicates the colloidal particle size in the solution. (B) XRD pattern of control perovskite film and film with (t-Bu)$_2$PMeHBF$_4$. (C) Gibbs free energies of perovskite nucleation with and without seed. (D) Schematic illustration of hetero-seeding induced crystallization (hetero-SiC) by (t-Bu)$_2$PMeHBF$_4$.

To demonstrate the nucleation process, the perovskite precursor inks with and without (t-Bu)$_2$PMeHBF$_4$ (0.3% mol) are prepared and dropped onto ITO substrates followed by 70 ^{o}C thermal annealing. The whole nucleation and crystallization process is recorded by an optical microscope camera in real-time. The video frames at 0s, 20s, 25s, and 30s are grabbed and shown in Fig. S3. The scale bar in the frames is 300 μm. Initiated from 0s, both two precursor droplets are clear. After 20s, a large amount of small black perovskite crystals appears in the precursor with (t-Bu)$_2$PMeHBF$_4$, while only a few crystals are formed in the control one. With the time going on (25s and 30s), this difference between the two precursors becomes prominent and the perovskite crystals with (t-Bu)$_2$PMeHBF$_4$ grow much larger, which indicated a faster crystallization process by hetero-SiC. This is because hetero-SiC could facilitate the nucleation process at nucleation sites (nuclei of (t-Bu)$_2$PMeHBF$_4$-PbI$_2$ complex), in contrast to homogeneous nucleation (control precursor).

Besides the faster hetero-SiC nucleation process in the liquid phase, we also observe a faster crystallization process for the film prepared by a one-step spin-coating process (same as the device), characterized by in-situ absorption measurement. The in-situ absorption spectra show an absorption redshift at ~ 10s in both the control film and the film with (t-Bu)$_2$PMeHBF$_4$ (0.3% mol) during the 120 ^{o}C annealing process (**Fig. 2A**). The as-casted intermediate film exhibits only UV absorption at wavelengths shorter than 450 nm which is attributed to the solvent complex. During the annealing process, the absorption at wavelengths longer than 450nm gradually increases, which is due to the phase transition from the intermediate phase and enhanced crystallinity of perovskite grain. In comparison with the control film, the film with (t-Bu)$_2$PMeHBF$_4$ exhibits a faster crystallization process where the time of film absorption reaching the peak is 10s earlier than the control film. To quantify the difference between the two films, the in-situ absorption color mapping is further interpreted by extracting the absorption intensity at the wavelength of 550 nm and plotting the absorption intensity as a function of annealing time in **Fig.2B**. XRD measurements are also conducted to investigate the perovskite phase transition, shown in **Fig. 2C** and **2D**. The XRD patterns are collected from different annealing times (0s, 3s, 5s, 10s, 15s, 20s, 30s, 60s, 3min, 5min, and 10min). Before thermal annealing, two intermediate films (0s) both exhibit three main peaks (denotes by & in the figure) at 6.6^o, 7.2^o, and 9.2^o which are corresponding to (002), (021), and (022) planes of MAI-PbI$_2$-DMSO intermediate phase (**Fig. 2C** and **2D**).[5, 35, 36] Compared with hetero-SiC film, the control film exhibits much stronger diffraction peaks of non-perovskite phase (δ-FAPbI$_3$) and PbI$_2$ (001) at 11.8^o and 12.8^o, respectively. This indicates the addition of (t-Bu)$_2$PMeHBF$_4$ could effectively suppress the formation of δ-FAPbI$_3$ in the intermediate stage. From the SEM images of the intermediate phase, the hetero-SiC film exhibits larger perovskite

crystal grains with a clear grain boundary, while the control intermediate film shows lots of small grains without a clear grain boundary (fig. S4). The white spots on the two films are the gold cluster which is from the gold deposition before SEM measurement to enhance the film conductivity for a better SEM quality. The different morphology of the two intermediate films could be attributed to the faster crystallization process by the hetero-SiC process.

After thermal annealing, the phase conversion process from the intermediate phase to the perovskite phase is very fast.[35] From the XRD measurement (**Fig. 2C** and **2D**), we find the majority of the intermediate phase and δ-FAPbI$_3$ phase are converted into the perovskite phase at the first 3s. With the annealing process going on (3s and 5s), a small peak at 8.8^o is found in the hetero-SiC film which is corresponding with the complex of (t-Bu)$_2$PMeHBF$_4$-PbI$_2$. While for the intermediate film (0s), it is hard to distinguish the complex diffraction peak with (022) planes of the MAI-PbI$_2$-DMSO intermediate phase as they are overlapped with each other. With a longer annealing process, the complex of (t-Bu)$_2$PMeHBF$_4$-PbI$_2$ is gradually reduced (after 5s). This explains why we cannot find the peak of the complex from the XRD pattern of well-formed hetero-SiC perovskite film (**Fig. 2E**). At the first 10s, most of the residual solvent is evaporated and the intermediate phase is almost converted into the perovskite phase. With the removal of residual solvent and conversion of intermediate phase (MAI-PbI$_2$-DMSO), the absorption intensities of the two films gradually increase (**Fig. 2B**). After 10s, the absorption intensities increase much faster which could be attributed to a faster crystal growth after solvent evaporation. Compared with the control film, the hetero-SiC film also exhibits a much faster crystallization process (**Fig. 2B**). From the in situ XRD patterns, no big difference is observed which implied the phase transition is not the dominant factor of the increasing absorption (**Fig. 2C** and **2D**). From the SEM images, the dissolution and merging process of small particles into large crystals are observed (fig. S4).[2] The fast perovskite crystal growth plays the dominant role in absorption changing. At last, the increase of the film absorption intensity becomes lower.

The complete perovskite films are obtained after 1h thermal annealing. The grazing-incidence wide-angle x-ray scattering (GIWAXS) and X-ray diffraction (XRD) measurements are conducted onto the films with and without (t-Bu)$_2$PMeHBF$_4$ (annealing for 60 min) to investigate the crystallographic structure (**Fig. 2F**). From the GIWAXS map, two films exhibit the same patterns with two diffraction rings located at q of 0.9 Å^{-1} and 1 Å^{-1}, which is corresponding with the PbI$_2$ phase and perovskite (100), respectively. From the XRD patterns (**Fig. 2E**), we also find the same patterns of two films with the dominant peaks located at 12.65^o, 13.95^o, 24.45^o, and 28.2^o. These peaks are corresponding with the PbI$_2$, (100), (111), and (200) of FAPbI$_3$ perovskite crystal planes, respectively. With the well-controlled content of (t-Bu)$_2$PMeHBF$_4$, the hetero-SiC film exhibits the same crystallographic structure and same crystal orientation as the control film indicating the faster seeding-induced crystallization does not change the original perovskite crystallographic (**Fig. 2E** and **2F**). At last, we have also noticed interesting phenomenon. The PbI$_2$ peak is found from the GIWAXS map and XRD patterns for the film with 60 min annealing, while negligible PbI$_2$ Peak is generated at first 10 min annealing (Fig. C and D). In order to figure it, we then investigate the film annealing for 30 min and 50 min. With the increasing of annealing time

(from 30 min to 50 min), PbI$_2$ peak intensity is gradually increase (fig.Figure S5Sx). This is possible due to the evaporation of MACl during longer time annealing.
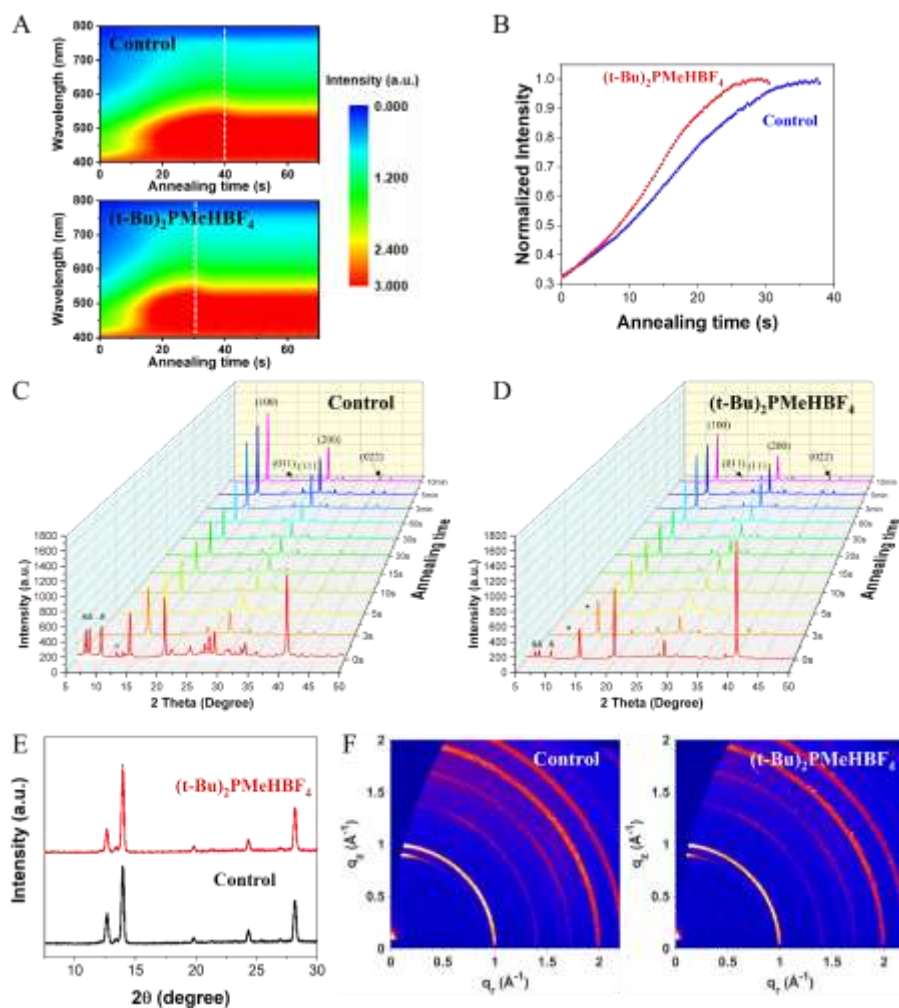

Fig. 2. In situ investigation of perovskite crystallization process by hetero-SiC approach ((t-Bu)$_2$PMeHBF$_4$). (A) In situ UV-vis absorption spectra as a function of annealing time for the control perovskite film and film with 0.3 mol % (t-Bu)$_2$PMeHBF$_4$ at 120°C. (B) UV-vis absorption intensity at the wavelength of 550 nm as a function of annealing time. In situ XRD measurement of (C) control perovskite film and (D) film with (t-Bu)$_2$PMeHBF$_4$ for different annealing times (0s, 3s, 5s, 10s, 15s, 20s, 30s, 60s, 3min, 5min, and 10min), & denotes the peaks of intermediate phase

8

and σ denotes the peak of σ-FAPbI₃. (E) Typical XRD patterns and (F) GIWAXS maps of control film and film with (t-Bu)₂PMeHBF₄ annealing for 60 min.

The time-of-flight secondary-ion mass spectrometry (ToF-SIMS) is then conducted to investigate the chemical composition throughout the perovskite film (**Fig. 3B**). The signal of InO⁻ indicates the touching of the substrate during the sputtering etching. From the result of ToF-SIMS, we find a well-distribution of (t-Bu)₂PMeH⁺ throughout the entire perovskite film, while the BF₄⁻ is predominantly accumulated at the substrate which is consistent with the previous report that BF₄⁻ is tended to accumulate at the metal oxide-perovskite interface.[24] The uniform distribution of (t-Bu)₂PMeH⁺ also helps to facilitate the perovskite crystallization of the entire film. The cross-section and top-view FESEM images of control film and hetero-SiC film are shown in **Fig. 3C** and **3D**. Compared with control film, the annealed hetero-SiC film exhibits a greatly enlarged grain size (largest one is around 2um), while the grain size of annealed control film is around 1 um for the largest grain. For a precise analysis, the grain size distribution is obtained from Fig D and Figure S5 D. The average grain size of control film is around 0.92 um. The perovskite grain size becomes larger with (t-Bu)2PMeHBF4, where the average grain size of films with 0.3% and 0.5% (t-Bu)2PMeHBF4 are 1.49 um and 1.7 um, respectively (Figure fig. S6x). From the cross-section FESEM images, the film with (t-Bu)₂PMeHBF₄ also exhibits a compact and smooth grain with enlarged grain size. The cross-section view SEM image of the control film also shows a smaller grain size with a clear grain boundary which is consistent with the top-view FESEM image. The FESEM image demonstrates the hetero-SiC approach could effectively facilitate the perovskite crystallization and lead to a high-quality perovskite film with enlarged grain size (**Fig. 3A**).[10, 21]

In addition, we also prepare types of related chemicals into the precursor to further study the proposed mechanism, including KBF₄, NaBF₄, and (t-Bu)₂PMe. However, with the addition of the above-mentioned chemicals (from 0.1% mol to 5% mol), no precipitate is found in the perovskite precursors. The FESEM measurement is then conducted onto the films with these additives. The morphologies of control film and films with KBF₄, NaBF₄, or (t-Bu)₂PMe are very similar and no enlarged grain sizes are found (fig. S5S7). However, the film with the (t-Bu)₂PMeHBF₄ exhibits an obvious enlarged grain size. This could be due to the KBF₄, NaBF₄, and (t-Bu)₂PMe cannot form low solubility seeds in the precursor, which further proves the function of seeding (hetero-SiC process) on the film morphology.
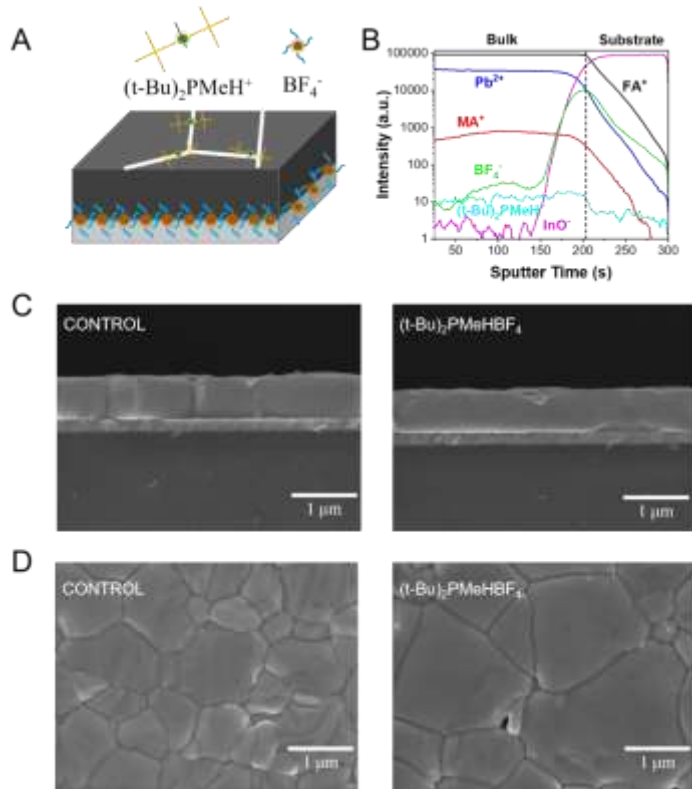
Fig. 3. Perovskite film processing and precisely growth modulation through (t-Bu)$_2$PMeHBF$_4$. (A) Schematic of synergetic effect of (t-Bu)$_2$PMeH$^+$ and BF$_4^-$ over the perovskite film. (B) Time-of-Flight Secondary Ion Mass Spectrometry (ToF-SIMS) of (t-Bu)$_2$PMeH$^+$ and BF$_4^-$ in the perovskite film. FESEM images of control film and film with (t-Bu)$_2$PMeHBF$_4$ for (C) cross-section view and (D) top-view.

To demonstrate the potential of the hetero-SiC approach on PSCs, the PSCs with the conventional structures are fabricated (glass/ITO/SnO$_2$/perovskite/Spiro-OMeTAD/Au). The performances of PSCs with and without (t-Bu)$_2$PMeHBF$_4$ are shown in **Fig. 4A** and **Table 1**. The optimized performance of PSCs is obtained with 0.3 % mol (t-Bu)$_2$PMeHBF$_4$, yielding a PCE of 24.0% with a short circuit current (J$_{SC}$) of 24.9 mA cm^{-2}, and open-circuit voltage (V$_{OC}$) of 1.19 V, and an excellent fill factor (FF) of 81%. In comparison, the control device exhibits a PCE of 22.2%, J$_{SC}$ of 24.4 mA cm^{-2}, V$_{OC}$ of 1.15 V, and FF of 77%. The hetero-SiC device exhibits great enhancement on both Voc (40 mV increasing) and FF (from 77% to 81%). The statistical distribution of the photovoltaic parameters is obtained from 20 individual cells of each type (fig. S6S8). The statistical results also demonstrate a better reproducibility of the V$_{OC}$ and FF enhancement via the hetero-SiC approach where the reproducibility of devices is critical in the practical

manufacturing process. The good repeatability by hetero-SiC could be attributed to the seeding guided growth rather than a random homogeneous crystallization. The corresponding forward-reverse direction J-V scans are shown in **Fig. 4B** and exhibit a negligible hysteresis for both two devices. The hetero-SiC approach also leads to stable steady-state power output (SPO) of 23.7% which is higher than the SPO of the control device (21.9%) (**Fig. 4C**). The corresponding external quantum efficiency (EQE) yields an integrated J_{SC} of 23.5 mA cm^{-2} for the control device and 23.8 mA cm^{-2} for the hetero-SiC device, which is in good agreement with the values from J-V curves (within 5% deviation). From the EQE measurement (**Fig. 4D**) and UV absorption (**Fig. 4D** inset), the hetero-SiC film exhibits the same bandgap as the control device (1.54 eV). Additionally, the dependence of V_{OC} and J_{SC} on the light intensity from 1 to 100 mW cm^{-2} is examined. The J_{SC} versus light intensity curves on a double-logarithmic scale (**Fig. 4E**) can be fitted according to the relation of $J_{SC} \propto \Phi^{\alpha}$, where Φ is the light intensity and α is the exponent. The calculated α values are 0.99 for the control, and 1.0 for the hetero-SiC PSCs, respectively. From the V_{OC} vs. light intensity curves (**Fig. 4F**), the V_{OC} is proportional to the logarithm of light intensity, and the slopes are calculated to be 1.89 K_BT/q for the control and 1.3 K_BT/q for the hetero-SiC PSCs, respectively, where K_B is the Boltzmann constant, T is the absolute temperature in Kelvin and q is the elementary charge. The enhanced slope of hetero-SiC PSCs indicates the hetero-SiC could significantly suppress the trap-assisted recombination and reduce the V_{OC} loss.

The electronic structure of the control film and hetero-SiC film are investigated via ultraviolet photoelectron emission spectra (UPS), shown in **Fig. 4G**. The highest occupied VB level, CB level, and work function (WF) are calculated and shown in **Fig. 4G** inset. It is noted that the VB level for hetero-SiC perovskite film changed to -5.6 eV from -5.7 eV (control film). The increased VB level of hetero-SiC reduces the energy barrier with spiro-OMeTAD (5.22 eV) which enhances the hole collection rates and block undesirable electron transfer from the perovskite to the spiro-OMeTAD. The photoluminescence (PL) spectroscopy is then conducted on the perovskite films to investigate the charge carrier dynamics (**Fig. 4H** and **4I**). From the steady-state PL spectra of perovskite films, the hetero-SiC film exhibits a threefold enhancement over the control film indicating the suppression of recombination via the hetero-SiC approach (**Fig. 4H**). The time-resolved PL (TRPL) decay profiles (**Fig. 4I**) were fitted via a bi-exponential decay model ($Y = A_1\exp(-t/\tau_1) + A_2\exp(-t/\tau_2)$), where τ_1 and τ_2 denote the fast and slow decay time constants, relating to the radiative and trap-assisted nonradiative recombination processes, respectively. Compared to the control film, the hetero-SiC film demonstrates a great enhancement in both τ_1 (560.3 ns Vs 78.8 ns) and τ_2 (1710.2 ns Vs 351.8 ns). The TRPL results also demonstrate a great suppression of trap-assisted non-radiative recombination and the lowest defect density of perovskite film by the hetero-SiC approach which is consistent with the 40 mV Voc enhancement. Based on the previously results, the enhancement of Voc and FF of hetero-SiC device can be ascribed to several factors. Firstly, the hetero-SiC process facilitates the perovskite crystallization and leading to an enlarged grain size and high crystal quality. The larger grain size could greatly reduce the grain boundaries which benefits the suppression of charge carrier recombination, resulting in a better performance.[27] Secondly, the reduced energy barrier between perovskite layer and spiro-OMeTAD facilitates the carrier collect rates. This is another important

reason for the increasing in Voc and FF.[31] Lastly, the passivation function of ionic salts plays an important role one performance enhancement, such as BF_4^-. [37]
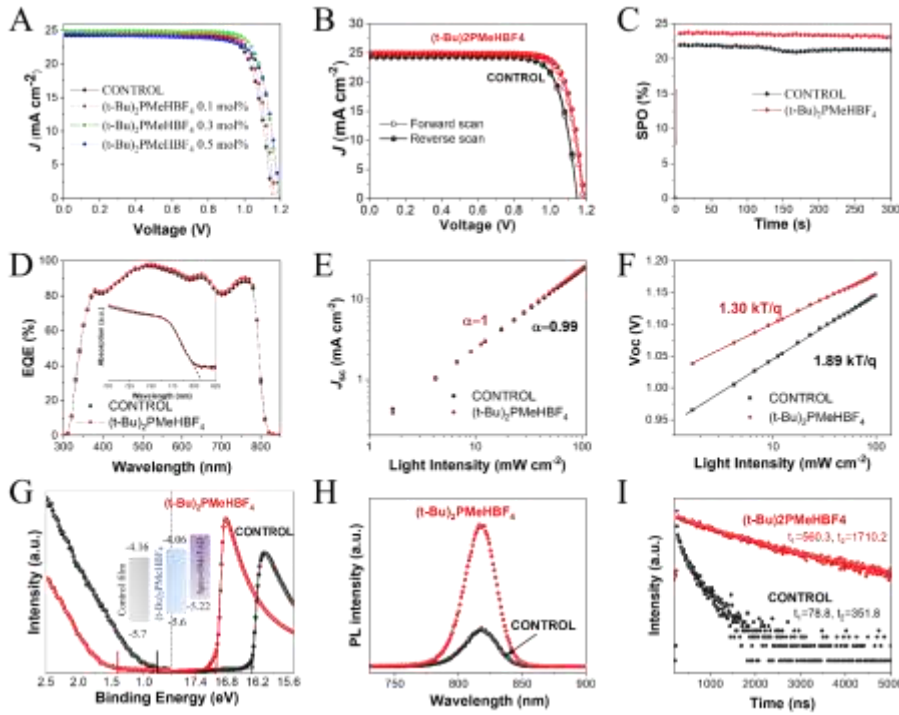
Fig. 4. Photovoltaic and optoelectronic properties of the control device and (t-Bu)₂PMeHBF₄ devices. J-V characterization of (A) control device and (t-Bu)₂PMeHBF₄ devices and (B) forward and reverse scan. (C)Steady-state output at the maximum power point of devices. (D) Corresponding external quantum efficiency (EQE) spectra of these cells. The light intensity-dependent of (E)J_{SC} and (F) V_{OC} for the control and (t-Bu)₂PMeHBF₄ device. (G) UPS of the control and (t-Bu)₂PMeHBF₄ perovskite films; inset: the energy level calculated from UPS spectra. (H) Steady-state photoluminescence (PL) and (I) time-resolved photoluminescence (TRPL) analysis of perovskite films with and without (t-Bu)₂PMeHBF₄.

Table 1. Photovoltaic parameters of the control device and devices with various concentrations of (t-Bu)₂PMeHBF₄, under simulated AM 1.5G irradiation at 100 mW cm⁻².

Device	V_{OC}(V)	J_{SC} (mA cm⁻²)	FF (%)	PCE (%)
Control	1.15	24.4	79	22.2
1mg mL⁻¹	1.17	24.5	80	22.9
3mg mL⁻¹	1.19	24.9	81	24.0

| 5mg mL^{-1}	1.19	24.4	77	22.4

Table 2. Photovoltaic parameters of the forward-scan and reverse-scan of the champion cells of the control device and device with (t-Bu)$_2$PMeHBF$_4$, under simulated AM 1.5G irradiation at 100 mW cm^{-2}.

Device		V_{OC} (V)	J_{SC} (mA cm^{-2})	FF (%)	PCE (%)
Control device	Forward scan	1.14	24.3	79	21.9
	Reverse scan	1.15	24.3	79	22.1
(t-Bu)$_2$PMeHBF$_4$ device	Forward scan	1.19	24.9	80	23.7
	Reverse scan	1.19	24.9	81	24.0

Currently, the PSCs are on the eve of commercialization and the stability of PSCs is the most urgent issue to be solved. The stability measurements are then conducted on control and hetero-SiC devices (**Fig. 5**). Ten devices for each group are prepared for the stability measurements. For storage stability, the non-encapsulated devices were stored in a dry box with 20–30% relative humidity (RH). Compared to the control cells, which maintain ≈82% of their initial PCE over 2300 h storage, the hetero-SiC devices exhibit much better storage stability (91% of their initial PCEs). Apart from the storage stability, the hetero-SiC devices also exhibit a great enhancement in both thermal stability and light stability. For thermal stability, the hetero-SiC devices maintain 77% of their original PCE over 1400h 80°C thermal annealing, while the control devices only keep 56% of their initial performance. And for the light stability, the hetero-SiC devices demonstrate better stability (84% of initial PCE) over 1400h continuous light soaking. In comparison, the control device only maintains 30% of initial PCE after 1400h light soaking which indicates the hetero-SiC devices have much better performance on long time operation, which could be attributed to the reduced defects of perovskite film via hetero-SiC and passivation of ionic anion and cation.

From the morphology characterization results, the hetero-SiC film exhibits an enlarged grain size which could greatly reduce the grain boundary density. The reduced grain boundary density can effectively prevent water dispersion over crystal grain. From fig. S7S9, two drops of water (2 ul, 1cm distance) are dropped onto the control film and hetero-SiC film at the same distance. The water droplets on the control film spread very fast and are merged. And the hetero-SiC perovskite film with enlarged grain size can prevent water droplets from spreading and maintain their shape. The static contact angles of water droplets on the two films are similar (59.8^o for the control film and 60.2^o for the hetero-SiC film). This is because a small amount of (t-Bu)$_2$PMeHBF$_4$ can just modify the crystallization process and has little influence on film hydrophobic property.

All in all, the hetero-SiC approach not only brings a device performance bosting but also a great improvement in device stability. The enhanced stability of the hetero-SiC device could be attributed to the enhanced film quality, enlarged grain size, and reduced defect density.
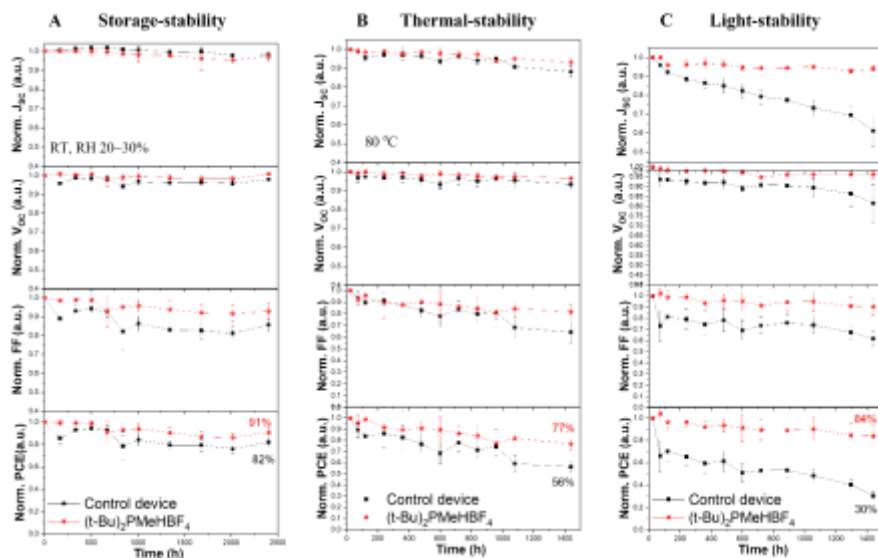
Fig. 5. Stability measurement of solar cells. (A) storage-stability, (B) thermal-stability and (C) light-stability.

Conclusion

In summary, we are the first group to report the seeding-induced crystallization approach for the one-step spin-coating perovskite fabrication method. The (t-Bu)$_2$PMeHBF$_4$ is added to the precursor which formed a low solubility complex with PbI$_2$. We take the advantage of the solubility difference between seeding material and perovskite material for the seed-induced crystallization. The seeds can effectively reduce the perovskite crystallization energy barrier and facilitate the growth of perovskite film. Combined with multiple in situ analysis tools, our reported hetero-SiC approach is proven to be one effective way to facilitate perovskite crystallization. The hetero-SiC films exhibit large grain sizes with reduced defects which results in PSCs PCEs with up to 24.0% and 40 mV V$_{OC}$ enhancement. Furthermore, the hetero-SiC PSCs also represent great stability over the control device: 91% of the initial PCE over 2300 h storage stability, 77% of the initial PCE over 1400 h 80°C thermal annealing, and 84% of the initial PCE over 1400 h light illumination. At last, the introduced hetero-SiC approach provides a meaningful practice to apply the classical theory (seeding-induced crystallization) in manipulating the perovskite growth which is an important exploration in the PSCs study.

Acknowledgements

Supporting Information

Experimental section

Material

The SnO_2 colloid precursor was purchased from Alfa Aesar. Formamidinium iodide (FAI), methylammonium bromide (MABr), and methylammonium chloride (MACl) were bought from Greatcell Energy. Di-tert-butyl(methyl)phosphonium tetrafluoroborate $((t\text{-}Bu)_2PMeHBF_4)$, cesium iodide (CsI), chlorobenzene (CB), acetonitrile (ACN), bis(trifluoromethane) sulfonimide lithium salt (Li-TFSI), 4-tertbutylpyridine (tBP), N, N-dimethylformamide (DMF), and dimethyl sulfoxide (DMSO) were obtained from Sigma-Aldrich. Spiro-OMeTAD, Lead iodide (PbI_2), and ITO substrates were purchased from Advanced Election Technology Co., Ltd. All chemicals were used without any further purification process.

Device Fabrication

The ITO glass was cleaned in detergent, deionized water, acetone, and isopropyl alcohol sequentially. After being dried by N_2 blowing, the cleaned ITO substrates were treated with ultraviolet ozone for 15 min to remove organic residues and enhance surface wetting. Then the prepared SnO_2 precursor (diluted by water with $SnO_2:H_2O=1:4$, v/v) was spin-coated onto the ITO substrates at 4000 rpm for 30 s, followed by thermal annealing at 150 °C for 30 min in ambient air. The ITO/SnO_2 samples were treated with ultraviolet ozone for 10 min before deposition of perovskite film. The perovskite precursor of $(FAPbI_3)_{0.93}(MAPbBr_3)_{0.04}(CsPbI_3)_{0.03}$ was prepared by dissolving 1.4M $FAPbI_3$, 0.06M $MAPbBr_3$, and 0.045M $CsPbI_3$ and 0.5M MACl into 1ml DMF/DMSO (8:1 v/v) solvent (10% excess PbI_2 was used to boost device performance) followed

by 2 hours mechanical shaking for the solution to clear. The perovskite precursor was then spin-coated onto ITO/SnO_2 by two consecutive spin-coating steps (1000 rpm 5 s and 5000 rpm 30 s). During the spin-coating process, the antisolvent of chlorobenzene was poured onto the perovskite film at 15 s. The intermediate phase film was annealed under 120 °C for 60 min in the glove box. After that, a thin layer of 2d perovskite was formed by coating BABr (3mg/ml in IPA) onto perovskite film at the speed of 5000 rpm, followed by a 10 min 100°C annealing process. Then, the hole transporting layer of 2,2′,7,7′-tetrakis (N, N-dip-methoxyphenylamine)-9,9′-spirobifluorene (Spiro-OMeTAD) was deposited onto the top of the perovskite layer by 3500 rpm for 30 s with the composition of 72.8 mg Spiro-OMeTAD, 18.8 μL bis(trifluoromethane) sulfonimide lithium salt (Li‑TFSI) stock solution (520 mg Li‑TFSI in 1 mL acetonitrile), 28.8 μL 4-tertbutylpyridine (tBP), and 1 mL chlorobenzene. Finally, 80 nm of Au was thermally evaporated as a counter electrode using a shadow mask. For the hetero-SiC approach, different amounts of (t-Bu)$_2$PMeHBF$_4$ are directly dissolved into the perovskite precursor solution. The rest steps are similar to the fabrication of control devices.

Characterizations and measurements

The XRD patterns of perovskite films were collected from Rigaku SmartLab 9KW-Advanced X-ray diffractometer with Cu Kα radiation in a step of 0.01° and θ-2θ scan mode. GIWAXS measurements were carried out with a Xeuss 2.0 SAXS/WAXS laboratory beamline using a Cu X-ray source (8.05 keV, 1.54 Å) and a Pilatus3R 300K detector. The incidence angle is 0.3°, except for the stated experiments. The FESEM images were collected from a field emission scanning electron microscope (Tescan VEGA3). The steady-state photoluminescence spectra and time-resolved photoluminescence were measured on the Edinburgh FLSP920 spectrophotometer equipped with the excitation source of 485 nm picosecond pulsed diode laser at an average power of 0.15 mW. The absorption spectra of perovskite films were measured by the UV-vis spectrophotometer (CARY5000, Varian). The PL measurement was conducted on an Edinburgh FLSP920 spectrophotometer equipped with a 485 nm picosecond pulsed diode. The X-ray photoelectron spectroscopy (XPS) and ultraviolet photoelectron spectroscopy (UPS) were measured from the X-Ray photoelectron spectrometer system (Thermo scientific Nexsa) equipped with a 12 kV aluminum Ka X-ray.

The in situ UV-vis absorption was measured by an F20 spectrometer (Filmetrics, Inc) with the light source of a halogen lamp (1.5 mm). A blank quartz substrate was used as the reference to calibrate the measurement signal. The absorbance of the thin film was calculated by the equation A=-$\log_{10}$(T), where the T is the transmission of the drying kinetics and crystallization rate of the perovskite thin film under ambient air conditions.[38] The in situ XRD and in situ SEM are also conducted from Rigaku SmartLab 9KW-Advanced X-ray diffractometer and field emission scanning electron microscope (Tescan VEGA3), where the detail measurement method is adopted from reference.[35]

Compositional depth profiling of perovskite films was carried out using a ToF-SIMS 5 system from IONTOF, operated in the spectral mode and using a 25-keV Bi^{3+} primary ion beam with an ion current of 0.7 pA. A mass-resolving power of about 8,000 m Δm^{-1} was reached. For depth

profiling, a 3-ke V Cs$^+$ sputter beam with a current of 28 nA was used to remove material layer by layer in interlaced mode, from a raster area of 300 μm × 300 μm. Mass spectrometry was performed on an area of 100 μm × 100 μm in the center of the sputter coater. A low-energy electron-flood gun was used for charge compensation. In the positive polarity, the [SnO + Cs]$^+$ secondary ion is the SnO fragment ionized through interaction with the sputter ion Cs$^+$, yielding the highest signal-to-noise ratio positive-secondary-ion signal characteristic of the ITO substrate.

The current-voltage (J-V) characteristic and steady-state power output of photovoltaic devices were measured by Keithley 2400 Source Meter under standard AM 1.5 G illumination using a solar simulator (Enli Tech, Taiwan), and the light intensity was calibrated by KG-5 silicon diode. The step voltage and scan speeds were 20 mV and 100 mV s^{-1}. The EQE measurement was carried out with an EQE system (Enli Tech, Taiwan) using 100 Hz chopped monochromatic light ranging from 300 nm to 900 nm.

Thermal-stability measurement was conducted by measuring the unencapsulated devices on an 80°C hot plate in the glove box. Photo-stability was measured using encapsulated devices under a white light-emitting diode array with the intensity equally with 0.8 suns AM 1.5G, calibrated by a standard silicon photodiode detector (equipped with a KG-5 filter).
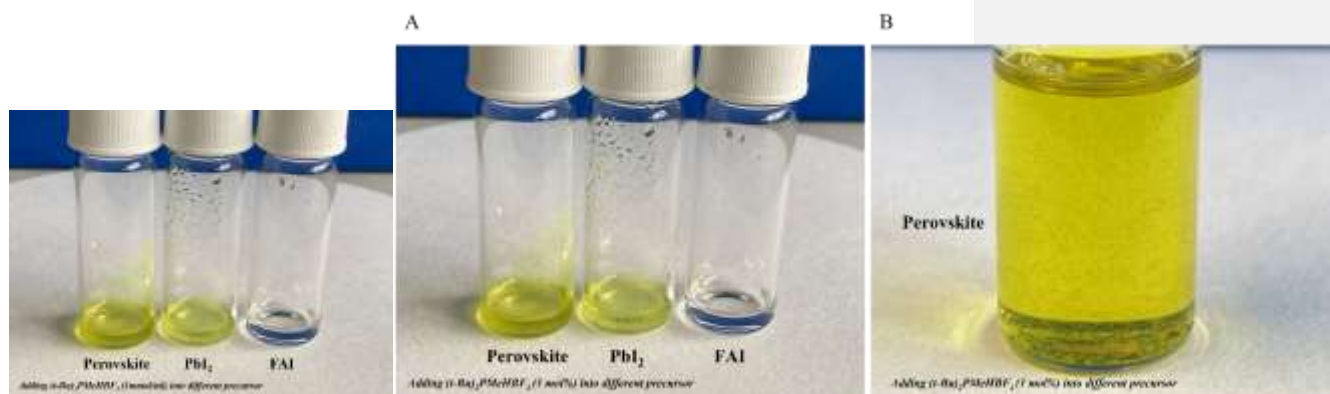

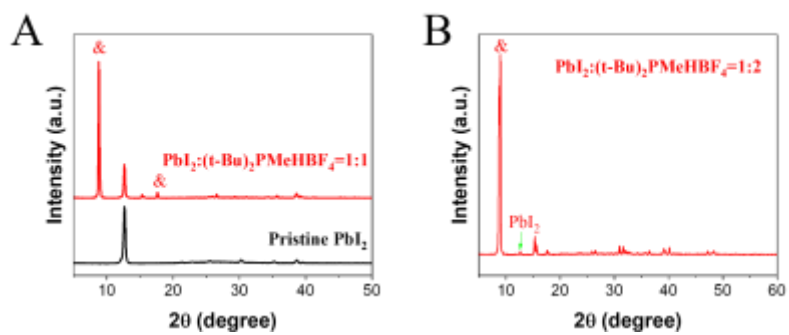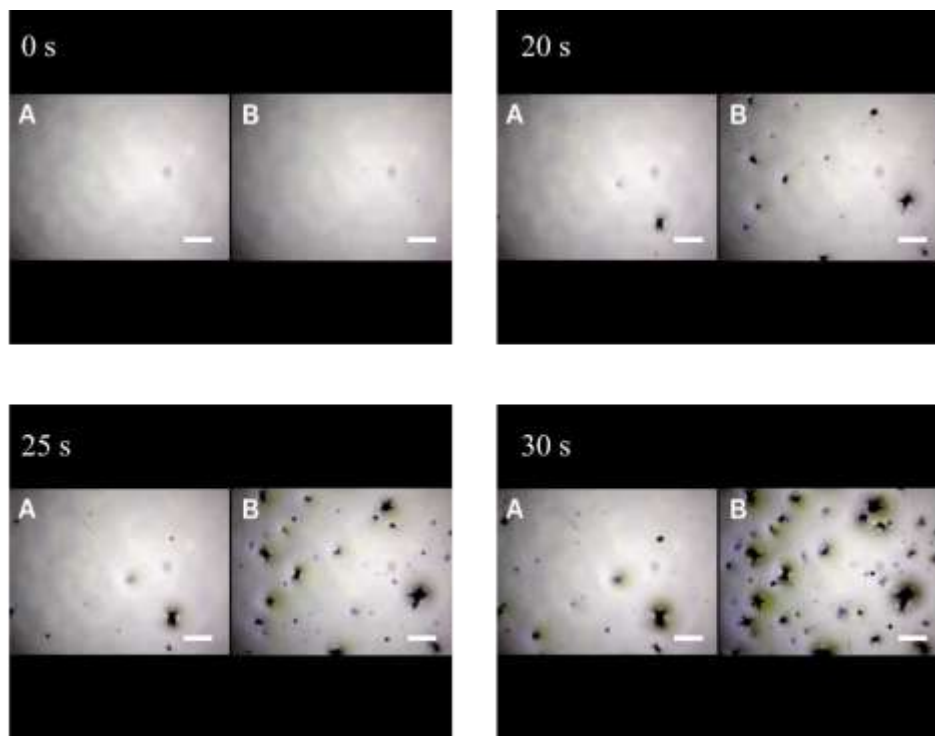Fig. S1. Optical image of precursor solution with 1% mol% (t-Bu)$_2$PMeHBF$_4$

Fig. S2. XRD patterns of PbI$_2$ with (t-Bu)$_2$PMeHBF$_4$ for different ratio (PbI$_2$:(t-Bu)$_2$PMeHBF$_4$): (A) 1:1 and (B) 1:2.

A: control, B: (t-Bu)$_2$PMeHBF$_4$

Fig. S3. Snapshots of the crystallization of precursor drop during 70 °C annealing process (scale bar-300 μm).
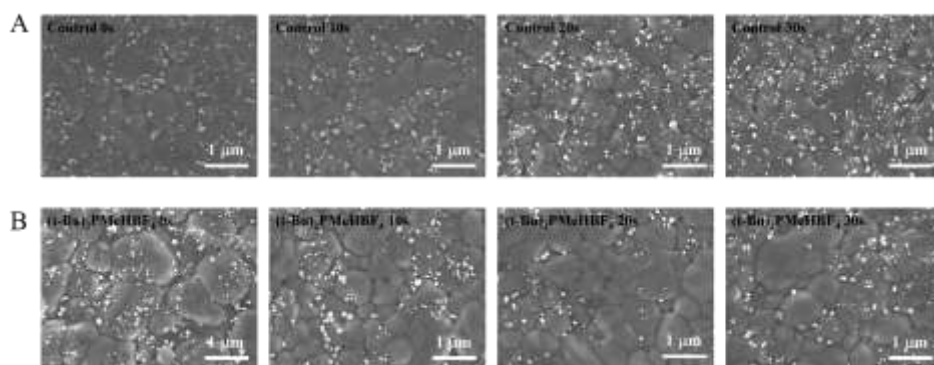

Fig. S4. SEM images of (A) control film and (B) film with (t-Bu)$_2$PMeHBF$_4$ annealing for different times (0s, 10s, 20s, and 30s).
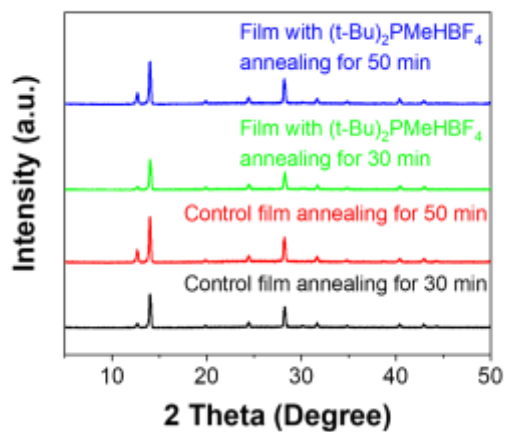

Fig. ure S5R2. : XRD of perovskite films with and without (t-Bu)$_2$PMeHBF$_4$ annealing for 30 min and 50 min.
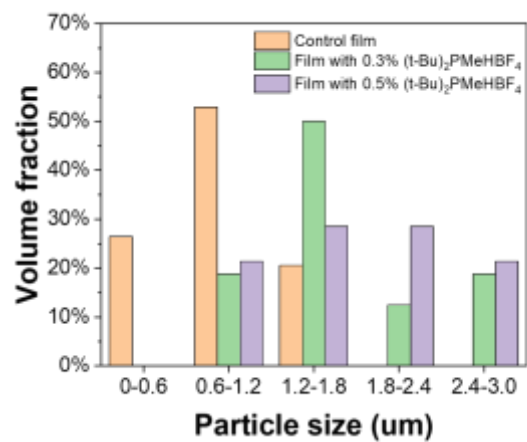
Fig.ure SR63. Grain size distribution of control film and film with $(t\text{-Bu})_2\text{PMeHBF}_4$
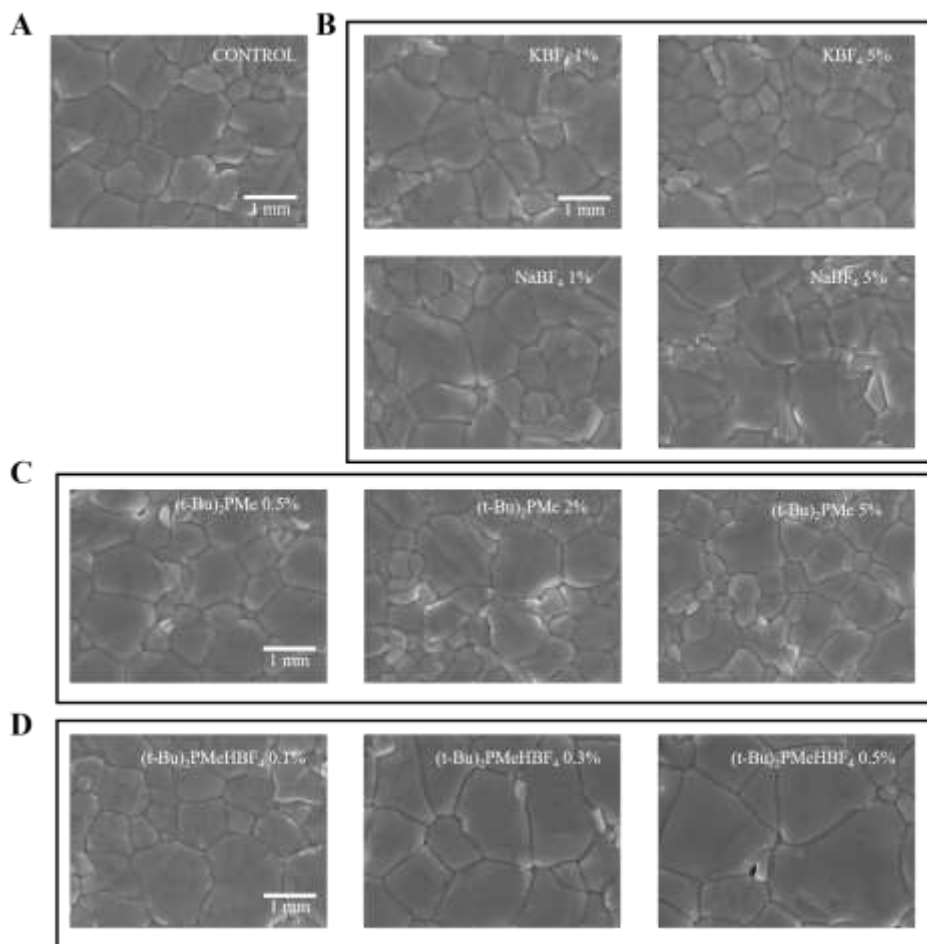
Fig. S5S7. Top view FESEM images of (A) control film, (B) film with KBF_4 and $NaBF_4$, (C) film with (t-Bu)$_2$PMe, and (D) film with (t-Bu)$_2$PMeHBF$_4$ of different concentrations.

Fig. S86. Statistical deviation of the photovoltaic parameters for the control devices and (t-Bu)$_2$PMeHBF$_4$ modulated devices (20 cells for each type): (A) J$_{SC}$, (B) V$_{OC}$, (C) Fill Factor, and (D) PCE.

Fig. S97. Contact angles of control film and film with (t-Bu)$_2$PMeHBF$_4$.

Figure R1. Optical image of perovskite precursor with 1% mol (t-Bu)$_2$PMeHBF$_4$

Reference

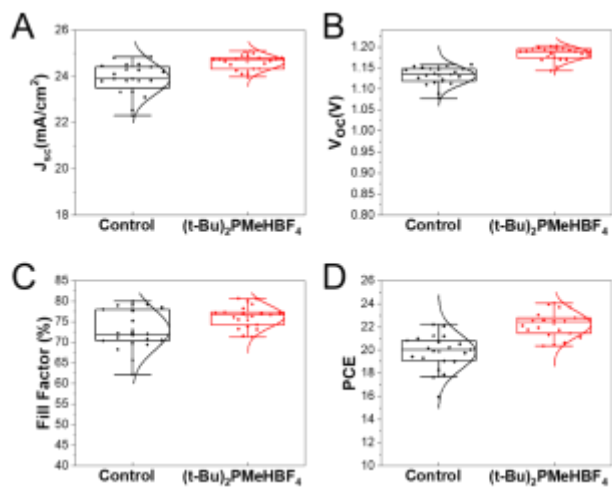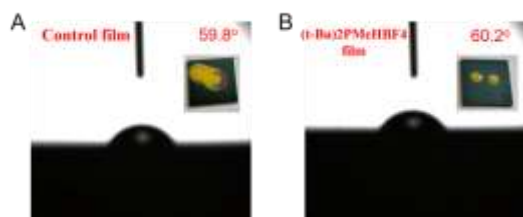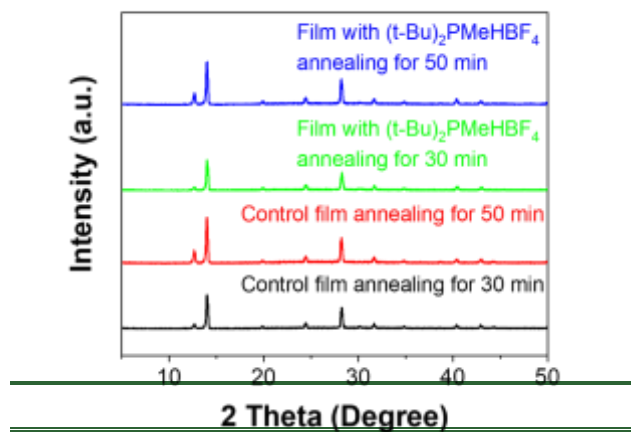1.   Green, M. A.; Dunlop, E. D.; Hohl-Ebinger, J.; Yoshita, M.; Kopidakis, N.; Bothe, K.; Hinken, D.; Rauer, M.; Hao, X., Solar cell efficiency tables (Version 60). *Progress in Photovoltaics: Research and Applications* **2022,** *30* (7), 687-701.

2.   Jung, M.; Ji, S.-G.; Kim, G.; Seok, S. I., Perovskite precursor solution chemistry: from fundamentals to photovoltaic applications. *Chemical Society Reviews* **2019,** *48* (7), 2011-2038.

3.   Xiao, M.; Huang, F.; Huang, W.; Dkhissi, Y.; Zhu, Y.; Etheridge, J.; Gray‑Weale, A.; Bach, U.; Cheng, Y. B.; Spiccia, L., A fast deposition‑crystallization procedure for highly efficient lead iodide perovskite thin‑film solar cells. *Angewandte Chemie International Edition* **2014,** *53* (37), 9898-9903.

4.   Hu, H.; Singh, M.; Wan, X.; Tang, J.; Chu, C.-W.; Li, G., Nucleation and crystal growth control for scalable solution-processed organic–inorganic hybrid perovskite solar cells. *Journal of Materials Chemistry A* **2020,** *8* (4), 1578-1603.

5.   Jeon, N. J.; Noh, J. H.; Kim, Y. C.; Yang, W. S.; Ryu, S.; Seok, S. I., Solvent engineering for high-performance inorganic–organic hybrid perovskite solar cells. *Nature materials* **2014,** *13* (9), 897-903.

6.   Huang, F.; Dkhissi, Y.; Huang, W.; Xiao, M.; Benesperi, I.; Rubanov, S.; Zhu, Y.; Lin, X.; Jiang, L.; Zhou, Y., Gas-assisted preparation of lead iodide perovskite films consisting of a monolayer of single crystalline grains for high efficiency planar solar cells. *Nano energy* **2014,** *10*, 10-18.

7.   Li, X.; Bi, D.; Yi, C.; Décoppet, J.-D.; Luo, J.; Zakeeruddin, S. M.; Hagfeldt, A.; Grätzel, M., A vacuum flash–assisted solution process for high-efficiency large-area perovskite solar cells. *Science* **2016,** *353* (6294), 58-62.

8.   Parambil, J. V.; Heng, J. Y. Y., Seeding in Crystallisation. In *Engineering Crystallography: From Molecule to Crystal to Functional Form*, Roberts, K. J.; Docherty, R.; Tamura, R., Eds. Springer Netherlands: Dordrecht, 2017; pp 235-245.

9.   Zhang, F.; Xiao, C.; Chen, X.; Larson, B. W.; Harvey, S. P.; Berry, J. J.; Zhu, K., Self-seeding growth for perovskite solar cells with enhanced stability. *Joule* **2019,** *3* (6), 1452-1463.

10.   Zhao, Y.; Tan, H.; Yuan, H.; Yang, Z.; Fan, J. Z.; Kim, J.; Voznyy, O.; Gong, X.; Quan, L. N.; Tan, C. S.; Hofkens, J.; Yu, D.; Zhao, Q.; Sargent, E. H., Perovskite seeding growth of formamidinium-lead-iodide-based perovskites for efficient and stable solar cells. *Nature Communications* **2018,** *9* (1), 1607.

11.   Zhang, W.; Xiong, J.; Li, J.; Daoud, W. A., Seed‐Assisted Growth for Low‐Temperature‐Processed All‐Inorganic CsPbIBr2 Solar Cells with Efficiency over 10%. *Small* **2020,** *16* (24), 2001535.

12.   Li, Q.; Zhao, Y.; Fu, R.; Zhou, W.; Zhao, Y.; Liu, X.; Yu, D.; Zhao, Q., Efficient Perovskite Solar Cells Fabricated Through CsCl‐Enhanced PbI2 Precursor via Sequential Deposition. *Advanced Materials* **2018,** *30* (40), 1803095.

13.   Zhang, H.; Liang, C.; Sun, M.; Sun, F.; Ji, C.; Wan, X.; Li, D.; You, F.; He, Z., Controlled Crystallization of CsRb‐Based Multi‐Cation Perovskite Using a Blended Sequential Process for High‐Performance Solar Cells. *Solar RRL* **2021,** *5* (5), 2100050.

14.   Alharbi, E. A.; Baumeler, T. P.; Krishna, A.; Alyamani, A. Y.; Eickemeyer, F. T.; Ouellette, O.; Pan, L.; Alghamdi, F. S.; Wang, Z.; Alotaibi, M. H., Formation of high‐performance multi‐cation halide perovskites photovoltaics by δ‐CsPbI3/δ‐RbPbI3 seed-assisted heterogeneous nucleation. *Advanced Energy Materials* **2021,** *11* (16), 2003785.

15.   Li, Q.; Zhao, Y.; Zhou, W.; Han, Z.; Fu, R.; Lin, F.; Yu, D.; Zhao, Q., Halogen engineering for operationally stable perovskite solar cells via sequential deposition. *Advanced Energy Materials* **2019,** *9* (46), 1902239.

16.   Zhang, J.; Bu, T.; Li, J.; Li, H.; Mo, Y.; Wu, Z.; Liu, Y.; Zhang, X.-L.; Cheng, Y.-B.; Huang, F., Two-step sequential blade-coating of high quality perovskite layers for efficient solar cells and modules. *Journal of materials chemistry A* **2020,** *8* (17), 8447-8454.

17.   Li, S.-S.; Chang, C.-H.; Wang, Y.-C.; Lin, C.-W.; Wang, D.-Y.; Lin, J.-C.; Chen, C.-C.; Sheu, H.-S.; Chia, H.-C.; Wu, W.-R., Intermixing-seeded growth for high-performance planar heterojunction perovskite solar cells assisted by precursor-capped nanoparticles. *Energy & Environmental Science* **2016,** *9* (4), 1282-1289.

18.   Lin, C. Y.; Li, S. S.; Chang, J. W.; Chia, H. C.; Hsiao, Y. Y.; Su, C. J.; Lian, B. J.; Wen, C. Y.; Huang, S. K.; Wu, W. R., Unveiling the Nanoparticle‐Seeded Catalytic Nucleation Kinetics of Perovskite Solar Cells by Time‐Resolved GIXS. *Advanced Functional Materials* **2019,** *29* (36), 1902582.

19.   Rana, P. J. S.; Febriansyah, B.; Koh, T. M.; Muhammad, B. T.; Salim, T.; Hooper, T. J.; Kanwat, A.; Ghosh, B.; Kajal, P.; Lew, J. H., Alkali Additives Enable Efficient Large Area (> 55 cm2) Slot‐Die Coated Perovskite Solar Modules. *Advanced Functional Materials* **2022**, 2113026.

20.   Xu, S.; Kang, C.; Huang, Z.; Zhang, Z.; Rao, H.; Pan, Z.; Zhong, X., Dual‐Functional Quantum Dot Seeding Growth of High‐Quality Air‐Processed CsPbI2Br Film for Carbon‐Based Perovskite Solar Cells. *Solar RRL* **2022,** *6* (4), 2100989.

21.   Bi, D.; Yi, C.; Luo, J.; Décoppet, J.-D.; Zhang, F.; Zakeeruddin, S. M.; Li, X.; Hagfeldt, A.; Grätzel, M., Polymer-templated nucleation and crystal growth of perovskite films for solar cells with efficiency greater than 21%. *Nature Energy* **2016,** *1* (10), 1-5.

22.   Shen, Z.; Han, Q.; Luo, X.; Shen, Y.; Wang, T.; Zhang, C.; Wang, Y.; Chen, H.; Yang, X.; Zhang, Y., Crystal-array-assisted growth of a perovskite absorption layer for efficient and stable solar cells. *Energy & Environmental Science* **2022,** *15* (3), 1078-1085.

23.   Lin, Y.-H.; Sakai, N.; Da, P.; Wu, J.; Sansom, H. C.; Ramadan, A. J.; Mahesh, S.; Liu, J.; Oliver, R. D.; Lim, J., A piperidinium salt stabilizes efficient metal-halide perovskite solar cells. *Science* **2020,** *369* (6499), 96-102.

24.   Bai, S.; Da, P.; Li, C.; Wang, Z.; Yuan, Z.; Fu, F.; Kawecki, M.; Liu, X.; Sakai, N.; Wang, J. T.-W., Planar perovskite solar cells with long-term stability using ionic liquid additives. *Nature* **2019,** *571* (7764), 245-250.

25.   Yang, D.; Zhou, X.; Yang, R.; Yang, Z.; Yu, W.; Wang, X.; Li, C.; Liu, S. F.; Chang, R. P., Surface optimization to eliminate hysteresis for record efficiency planar perovskite solar cells. *Energy & Environmental Science* **2016,** *9* (10), 3071-3078.

26.   Xia, R.; Gao, X. X.; Zhang, Y.; Drigo, N.; Queloz, V. I.; Tirani, F. F.; Scopelliti, R.; Huang, Z.; Fang, X.; Kinge, S., An Efficient Approach to Fabricate Air‐Stable Perovskite Solar Cells via Addition of a Self‐Polymerizing Ionic Liquid. *Advanced Materials* **2020,** *32* (40), 2003801.

27.   Yang, Y.; Wu, J.; Wang, X.; Guo, Q.; Liu, X.; Sun, W.; Wei, Y.; Huang, Y.; Lan, Z.; Huang, M., Suppressing vacancy defects and grain boundaries via ostwald ripening for high‐performance and stable perovskite solar cells. *Advanced Materials* **2020,** *32* (7), 1904347.

28.   Noel, N. K.; Habisreutinger, S. N.; Wenger, B.; Lin, Y. H.; Zhang, F.; Patel, J. B.; Kahn, A.; Johnston, M. B.; Snaith, H. J., Elucidating the Role of a Tetrafluoroborate‐Based Ionic Liquid at the n‐Type Oxide/Perovskite Interface. *Advanced Energy Materials* **2020,** *10* (4), 1903231.

29.   Li, M.; Zhao, C.; Wang, Z. K.; Zhang, C. C.; Lee, H. K.; Pockett, A.; Barbé, J.; Tsoi, W. C.; Yang, Y. G.; Carnie, M. J., Interface modification by ionic liquid: a promising candidate for indoor light harvesting and stability improvement of planar perovskite solar cells. *Advanced Energy Materials* **2018,** *8* (24), 1801509.

30.   Caprioglio, P.; Cruz, D.; Caicedo-Davila, S.; Zu, F.; Sutanto, A. A.; Pena-Camargo, F.; Kegelmann, L.; Meggiolaro, D.; Gregori, L.; Wolff, C. M., Bi-functional Interfaces by Poly-Ionic Liquid Treatment in Efficient pin and nip Perovskite Solar Cells. *Energy & Environmental Science* **2021**.

31.   Wang, X.; Wu, J.; Yang, Y.; Li, G.; Song, Z.; Liu, X.; Sun, W.; Lan, Z.; Gao, P., Chromium trioxide modified spiro-OMeTAD for highly efficient and stable planar perovskite solar cells. *Journal of Energy Chemistry* **2021,** *61*, 386-394.

32.   Mullin, J. W., *Crystallization*. Elsevier: 2001.

33.   Boistelle, R.; Astier, J., Crystallization mechanisms in solution. *Journal of Crystal Growth* **1988,** *90* (1-3), 14-30.

34.   Abraham, F. F., *Homogeneous nucleation theory*. Elsevier: 1974; Vol. 263.

35.   Chen, S.; Xiao, X.; Chen, B.; Kelly, L. L.; Zhao, J.; Lin, Y.; Toney, M. F.; Huang, J., Crystallization in one-step solution deposition of perovskite films: Upward or downward? *Science Advances* **2021,** *7* (4), eabb2412.

36.   Qin, M.; Tse, K.; Lau, T. K.; Li, Y.; Su, C. J.; Yang, G.; Chen, J.; Zhu, J.; Jeng, U. S.; Li, G., Manipulating the Mixed‐Perovskite Crystallization Pathway Unveiled by In Situ GIWAXS. *Advanced Materials* **2019,** *31* (25), 1901284.

37.   Niu, T.; Chao, L.; Gao, W.; Ran, C.; Song, L.; Chen, Y.; Fu, L.; Huang, W., Ionic Liquids-Enabled Efficient and Stable Perovskite Photovoltaics: Progress and Challenges. *ACS Energy Letters* **2021,** *6* (4), 1453-1479.

38.   Hu, H.; Ren, Z.; Fong, P. W.; Qin, M.; Liu, D.; Lei, D.; Lu, X.; Li, G., Room‐temperature meniscus coating of> 20% perovskite solar cells: a film formation mechanism investigation. *Advanced Functional Materials* **2019,** *29* (25), 1900092.